Acta Geotechnica (2021) 16:2609–2628
https://doi.org/10.1007/s11440-021-01297-4

RESEARCH PAPER

A 2D FDEM-based moisture diffusion–fracture coupling model for simulating soil desiccation cracking

Chengzeng Yan[1,2] · Tie Wang[1] · Wenhui Ke[3] · Gang Wang[2]

Received: 29 March 2021 / Accepted: 27 June 2021 / Published online: 13 July 2021

Abstract
Based on the combined finite–discrete element method (FDEM), this paper presents a moisture diffusion–fracture coupling model to simulate soil desiccation cracking. The coupling model, firstly, analyzes moisture content distribution within the soil according to a moisture diffusion model. Then, the shrinkage stress caused by the change of moisture content is calculated and applied to the system equation of FDEM. Finally, if a new crack is generated, the node sharing relationship and mesh of adjacent solid elements are updated for moisture diffusion calculation in the next time step. In this paper, examples of 1D moisture migration in the soil trip, shrinkage stress and deformation caused by the moisture reduce in the rectangular soil are studied. The simulation results agree well with analytical solutions, which verifies the correctness of the proposed model. Then, the model is used to simulate soil desiccation cracking process, and the crack evolution pattern in the numerical results is consistent with experimental results. Besides, several main factors affecting soil desiccation cracking are also investigated, including the elastic modulus, the moisture shrinkage coefficient, and the soil thickness. The moisture diffusion–fracture coupling model provides a new research tool for studying the mechanical mechanism of soil desiccation cracking.

Keywords Crack initiation · FDEM · Moisture diffusion · Moisture content · Propagation · Soil desiccation cracking

1 Introduction

Desiccation cracking in soil due to loss of moisture is a commonly occurred natural phenomenon, which is also a fundamental problem involving multiple disciplines such as geotechnical engineering, environmental engineering, mining engineering, and agricultural engineering. Soil desiccation cracking can cause severe damage to hydraulic structures, extensive cracking in roadbeds and landfill clay liners, triggering of slope sliding, and even decline in crop yields. For example, desiccation cracks were observed in dikes and dams that affected their stability [7, 82]. In slope engineering, soil desiccation cracking not only causes the loss of the cohesive effect of the soil but also provides channels for rainwater to infiltrate into the slope and thus aggravates the damage and instability of the slope [2, 9, 46, 59, 81]. Bronswijk et al. [3] indicated that soil desiccation cracking controls the transport speed of moisture solute and microorganism in the soil, which affects crop growth and production significantly.

With more frequent occurrence of extreme arid climates recently, there are more and more engineering problems caused by soil desiccation cracking. Therefore, it is urgent to develop effective quantitative methods to study the fundamental mechanism of desiccation cracking in soils.

At present, the study of soil desiccation cracking mainly includes two approaches: experimental study and numerical simulation. The experimental research mainly focuses on the shrinkage and cracking behavior of soil [16, 35, 41]. Tang et al. [48] studied the influencing factors of surface

✉ Gang Wang
gwang@ust.hk

Chengzeng Yan
yancz@cug.edu.cn

[1] Faculty of Engineering, China University of Geosciences, Wuhan 430074, China

[2] Department of Civil and Environmental Engineering, Hong Kong University of Science and Technology, Clear Water Bay, Hong Kong, SAR, China

[3] Wuhan Municipal Construction Group Co., Ltd, Wuhan 430023, China

shrinkage cracks in clayey soils, which revealed that sample size, boundary conditions, soil properties, temperature, and drying conditions all affect the crack initiation and propagation in soil. Then, Tang et al. [47] carried out drying experiments on saturated clay layers and found that most of the crack growth and volume shrinkage occur in the continuous evaporation period, while the sample is still saturated. Yu and El-Zein [80] carried out a drying test of the clay layer under high-temperature conditions and observed clear cracks. Jones et al. [15] and Sentenac et al. [43] used geophysical methods to map actual 3D topography of drying cracks under different environmental conditions. Li and Zhang [22] conducted a field study to investigate the crack patterns and related geometric parameters and indicated that the lengths and apertures of the cracks followed a lognormal distribution as expected. Li et al. [21] used a newly designed experimental device to study the moisture characteristic curve of silty clay cracking under both dry and wet conditions. The possible factors affecting crack pattern and geometry, such as depth, thickness, density, spacing, and aperture, are also investigated through experiment of soil desiccation cracking in situ [6, 19, 23]. These experiments revealed that crack initiation depends on the soil mineralogy, environmental conditions (temperature, relative humidity, rainfall), and the thickness of the clay layer. However, sample preparation and laboratory or field testing are often time-consuming and expensive in experiments, and the measurement of the parameters involved in the drying process is very complicated.

Numerical simulation is another alternative approach to study soil shrinkage and cracking. The numerical simulations for simulating the soil desiccation cracking can be divided into two categories: (1) continuum-based methods, such as the finite element method (FEM), the extended finite element method (XFEM); (2) discontinuum-based methods, such as the distinct/discrete element method.

In terms of continuum-based numerical methods, Konrad and Ayad [18] analyzed the crack propagation in clay under evaporation conditions using linear elastic fracture mechanics (LEFM). Mohammadnejad and Khoei [26] studied the crack propagation in porous media using the extended finite element method (XFEM). The method was also used by Vahab et al. [55] to simulate the formation of drying cracks in the soil. Sánchez et al. [42] studied the 3D desiccation soil crack networks using a mesh fragmentation technique. Pouya [36] proposed a finite element formulation for the hydraulic diffusion problem in porous materials with cracks and gave the weak formulation for the problem and the corresponding finite element equation including cracks and the contribution of cracks to the flow. Based on the cohesive zone model and finite element code, Pouya et al. [37] proposed an energy approach as a complement to the stress approach commonly considered for investigating soil desiccation cracking.

Although several numerical methods based on finite element methods and linear fracture mechanics have been proposed, the mechanism of soil desiccation cracking has not been explained clearly [1, 5, 38, 53]. Because the crack initiation and propagation involve the generation of discontinuities, it is difficult to use continuous methods to model the shrinkage and cracking behavior of soils. For example, the location of crack initiation in the finite element method is difficult to determine, which is usually set manually in advance to reproduce the basic characteristics of the crack pattern [34]. The cracking model based on fracture mechanics is still immature and usually only considers the growth of a single crack [1, 51]. Therefore, these continuum-based methods are difficult to simulate desiccation cracking of soil.

For the discontinuum-based numerical methods, Vo et al. [57] examined a discontinuous model comprising explicit cracks modeled as zero-thickness joint elements. The coupled hydromechanical diffusion and deformation processes in unsaturated soil, underlying soil desiccation and cracking, were considered and numerically modeled. Sima et al. [45] studied the effects of soil thickness, shrinkage coefficient, and micromechanical parameters on soil desiccation cracking using discrete element method (DEM). Yao and Anandarajah [79] proposed a three-dimensional discrete element model based on cuboid particles to analyze the shrinkage and cracking behavior of clayey soil. Gui and Zhao [11] and Gui et al. [12] used a discrete lattice spring model (DLSM) and Universal Distinct Element Code (UDEC) to simulate soil drying shrinkage and cracking, respectively. Tran et al. [54] combined the smooth particle hydrodynamics (SPH) method, size-dependent constitutive model and embedded cohesive fracture process zone to simulate soil desiccation cracking. Although PFC can solve complex cracking problems, the input parameters of PFC are difficult to calibrate, and the crack characterization is not intuitive [44]. It can be seen that some existing methods still have obvious disadvantages for simulating soil desiccation cracking.

To simulate transition from continua to discontinua, Munjiza et al. [27, 28, 30, 32] proposed the combined finite–discrete element method (FDEM) and developed an open-source research code, known as Y-Code [30], which combines the advantages of both continuum-based and discontinuum-based numerical methods and is very suitable for simulating solid fracturing [8, 72, 69]. Recent development in FDEM can be found in Rougier et al. [40], Munjiza et al. [33] and Fukuda et al. [10]. For example, Rougier et al. [39] developed a FDEM software package named Hybrid Optimization Software Suite (HOSS) for

simulation of fracturing of material. Lei et al. [20] and Munjiza et al. [31] developed an anisotropic deformation formula in FDEM for simulating the large deformation of geomaterials. Mahabadi et al. [25] conducted a three-dimensional FDEM numerical simulation of the fracturing process in the Opalinus Clay sample under the triaxial compression test. Tatone and Grasselli [49] proposed an approach to calibrate the microscopic parameters in FDEM for simulating rock fracturing. Munjiza et al. [33] developed a novel fluid–solid interaction solver for fracturing and fragmenting solids. Deng et al. [4] calibrated the value of normal contact penalty in FDEM and indicated that when the ratio of normal contact penalty to fracture penalty is 0.1448, the triangular elements can achieve a smooth transition from cohesion to contact.

It should be noted that FDEM can only perform purely mechanical fracture calculations initially. Recently, Yan et al. developed a series of hydromechanical [60, 62, 66, 73–75, 78], thermomechanical [61, 63, 67–71, 76], contact heat transfer [77] and hydrothermal coupling models [64, 65] into FDEM, which makes it an ideal model to simulate multiphysics-driven fracturing problems. However, to date, FDEM has not been used to simulate moisture diffusion, shrinkage and cracking of the soil. Therefore, we propose a two-dimensional moisture diffusion model to consider moisture transport in the soil in this paper. Moreover, the moisture diffusion model is combined with the FDEM mechanical fracture calculation to construct a coupled moisture diffusion–fracture model. The coupled model can simulate the moisture migration in the soil and soil desiccation cracking, which provides a new tool for studying the mechanism of shrinkage and cracking evolution in the soil.

2 Fundamentals of FDEM

The fundamental theory of FDEM is illustrated in Fig. 1. For 2D FDEM, the continuum is discretized into triangular finite element meshes, and a zero-thickness joint element with bonding effect is inserted on the common edge of adjacent elements. The crack initiation and propagation in the continuum are simulated by the joint element breaking, while the deformation of the continuum is simulated through the constant strain triangular element. The fracture criterion (mode I, mode II, and mixed mode) of the joint element is shown in Fig. 2. The detailed introduction of this method can be found in the literature [24, 29, 62, 65].

3 Coupling of moisture diffusion and mechanical fracture

Many researchers have studied the desiccation cracking mechanisms in clayey soils [14, 17, 58]. The thickness of the absorbed water film on the surface of clayey soil particles becomes thinner when the clayey soil loses moisture during drying, which shows the volume shrinkage at the macro-scale. The shrinkage deformation is affected by two factors: one is boundary constraint; the other is heterogeneous change of moisture in the clayey soil. Normally, the moisture change gradually decreases from the soil surface to the interior and thus the shrinkage deformation of the soil also decreases from the surface to the inside. The largest shrinkage deformation occurs at the surface of the soil layer. As the shrinkage deformation of the surface soil is restricted by the inner soil, tensile stress is generated at the soil surface. If the tensile stress exceeds the tensile strength of the soil, cracks are generated in the soil surface and extend inward.

In summary, two problems need to be solved in the study of soil desiccation cracking. The first is the moisture diffusion in the soil, and the second is the simulation of soil cracking. On the one hand, moisture diffusion can induce soil cracking, on the other hand, the soil cracking affects moisture migration. Therefore, in this study, we develop a moisture diffusion–fracture coupling model to simulate two-dimensional desiccation cracking phenomenon.

To simulate the soil desiccation cracking effectively, firstly, a 2D moisture diffusion model is established to

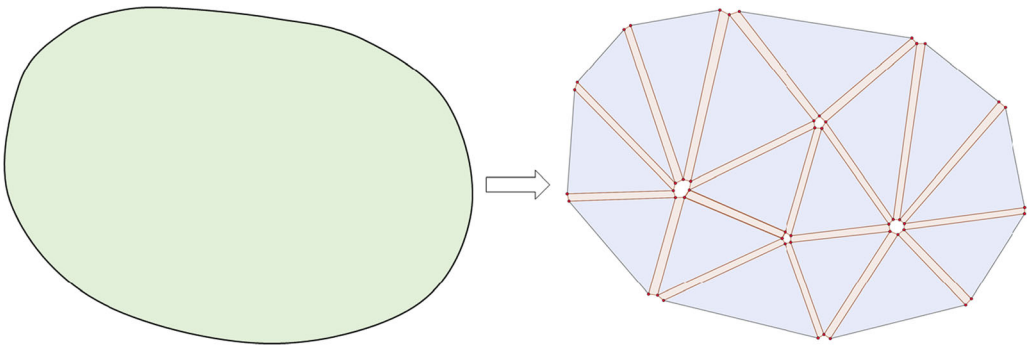

Fig. 1 Continuum characterization in 2D FDEM

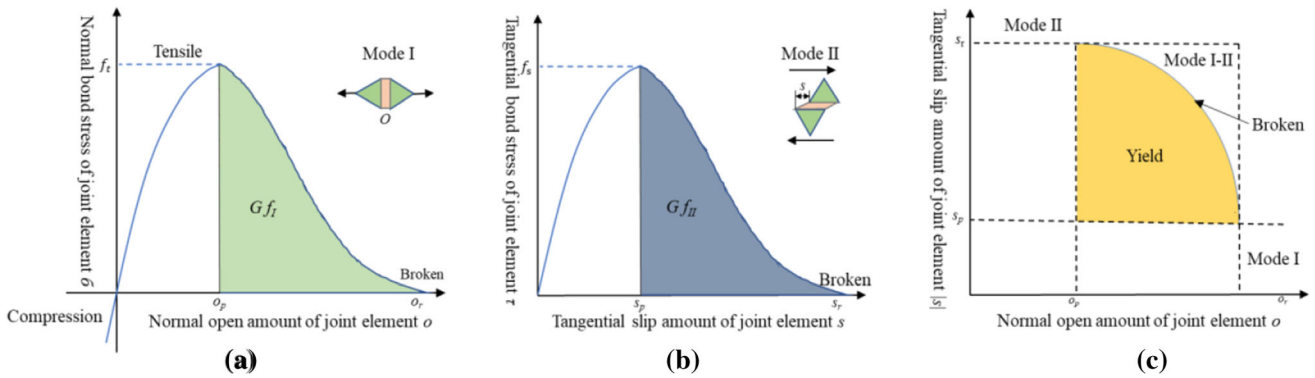

Fig. 2 Constitutive behavior of a joint element in 2D FDEM. **a** Relationship between normal bonding stress and normal opening amount in mode I; **b** relationship between tangential bonding stress and tangential slipping amount in mode II; **c** relationship between joint element yielded, failure and the normal opening amount and tangential slipping amount in mixed modes I–II

calculate the distribution and evolution of moisture content in the soil. Secondly, the cracking process is simulated by taking advantage of the FDEM capability. Next, the node sharing relationship between the adjacent triangular elements on both sides of the newly generated cracks is updated, which is used as the input of moisture migration calculation in the next time step to consider the discontinuity of moisture content across the crack. Finally, the coupled calculation of the moisture field, stress field, and fracturing is realized, and the whole process of soil desiccation cracking is simulated.

3.1 Moisture diffusion model

As shown in Fig. 3, the continuum is discretized into finite triangular elements in the moisture diffusion model. Thus, the distribution of the moisture content in the whole continuum can be expressed by the moisture content of each triangular element node. The moisture content in the triangular element can be obtained by linear interpolation. Taking node 1 as an example, six triangular elements Δ123, Δ134, Δ145, Δ157, Δ178, and Δ182 connect to node 1. Because the moisture content of node 1 may be different from that of nodes 2, 3, 4, 5, 7, and 8, the moisture may migrate in these triangular elements. Taking Δ123 as an example, the moisture content at its three nodes is w_i (i is the node number, i = 1, 2, 3). Assuming that the moisture content in a triangular element obeys a linear distribution, then the moisture gradient in the triangular element is a constant and can be expressed by

$$\frac{\partial w}{\partial x_i} = \frac{1}{A}\int_A \frac{\partial w}{\partial x_i} \mathrm{d}A \tag{1}$$

According to the Gaussian divergence theorem, Eq. (1) can be written as:

$$\frac{\partial w}{\partial x_i} = \frac{1}{A}\int_s w n_i \mathrm{d}s = \frac{1}{A}\sum_{m=1}^{3} \bar{w}^m \in_{ij} \Delta x_j^m \tag{2}$$

where A is the area of the triangular element, n_i is the external normal vector, $\bar{w}$ is the average moisture content of edge m, Δx_j^m is the difference between the coordinate components of the two vertices of edge m, and $\in_{ij}$ is the two-dimensional permutation tensor, $\in = \begin{pmatrix} 0 & 1 \\ -1 & 0 \end{pmatrix}$.

Assuming that the moisture migration in the triangular element is proportional to the moisture gradient, and the moisture flow per unit area along the i direction is given by

$$m_i = k_{ij}\frac{\partial w}{\partial x_i} \tag{3}$$

Substituting Eq. (2) into Eq. (3), the moisture flow m_x, m_y along the x, y direction per a unit area can be obtained.

Thus, the moisture mass into node 1 through Δ123 per unit time can be calculated by

$$M_{\Delta 123 \to 1} = -\frac{m_i n_i^{(1)} L^{(1)}}{2} \tag{4}$$

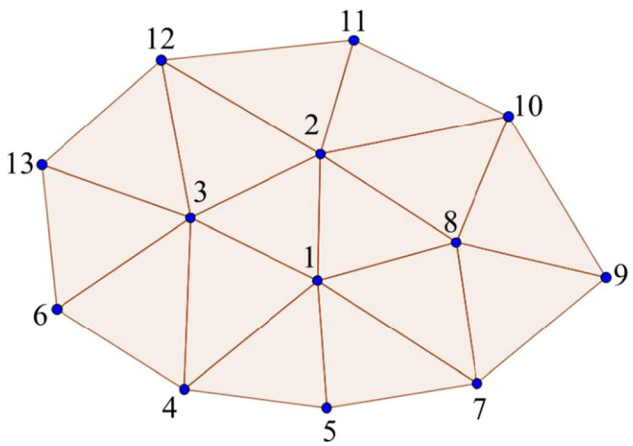

Fig. 3 Schematic diagram of moisture diffusion calculation

where $n_i^{(1)}$ is the outer normal unit vector of the edge opposite to node 1 in the triangular element, and $L^{(1)}$ is the length of the edge opposite to node 1.

In the same way, we can obtain the moisture mass $M_{\Delta 123\to 1}$, $M_{\Delta 134\to 1}$, $M_{\Delta 145\to 1}$, $M_{\Delta 157\to 1}$, $M_{\Delta 178\to 1}$, $M_{\Delta 182\to 1}$ into node 1 from the triangular elements Δ123, Δ134, Δ145, Δ157, Δ178 and Δ182.

Therefore, the moisture mass into node 1 per unit time is given by:

$$M_{\text{total}\to 1} = M_{\Delta 123\to 1} + M_{\Delta 134\to 1} + M_{\Delta 145\to 1} + M_{\Delta 157\to 1} + M_{\Delta 178\to 1} + M_{\Delta 182\to 1} \tag{5}$$

For any node i, the change of its moisture content can be written as:

$$\frac{\partial w_i}{\partial t} = \frac{M_{\text{total}\to i}}{M_s} \tag{6}$$

where M_s is the dry mass associated with the node i, M_{total} is the moisture mass into the node per unit time.

Combining Eqs. (5) and (6), the moisture content of node 1 can be updated by:

$$w_1^{t+\Delta t} = w_1^t + \frac{M_{\text{total}\to 1}\Delta t}{M_s} \tag{7}$$

where $w_1^{t+\Delta t}$ and w_1^t are the moisture content of node 1 at the next and the current time step, respectively.

According to the above steps, the moisture content of node 1 in the next time step is obtained. The moisture content of other nodes can be updated similarly. Note within a triangular element, the moisture mess is conserved, i.e.,

$$M_{\Delta 123\to 1} + M_{\Delta 123\to 3} + M_{\Delta 123\to 2} = 0 \tag{8}$$

3.2 Effect of crack propagation on moisture diffusion

Crack initiation and propagation change the moisture migration of the soil on both sides of the crack. After a crack is generated, the moisture cannot migrate directly from one side to the other side of the crack. Instead, the soil on both sides of the crack may exchange moisture with the air. Therefore, crack propagation will affect the calculation of moisture diffusion.

As shown in Fig. 4, a crack is generated within the soil mass of Fig. 3. The adjacent triangular elements on both sides of the crack are separated to consider the effect of crack propagation on moisture migration. For example, node 1 is separated into node 1 and node 1′; node 5 is separated into node 5 and node 5′. Δ123 and Δ128 are separated into Δ123 and Δ1′28, respectively; Δ145 and Δ157 are separated into Δ145 and Δ15′7, respectively. Thus, the moisture into node 1 from Δ128, Δ187, Δ175 becomes Δ1′28, Δ1′87, Δ1′75 flowing into node 1′. The moisture into node 1 has changed because only the moisture of Δ123, Δ134, Δ145 flows into node 1. Then, the moisture mass into node 1 per unit time through directly connected triangular elements can be updated as:

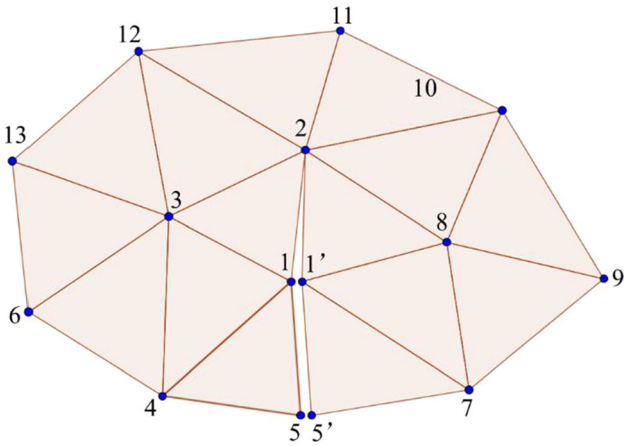

Fig. 4 The effect of crack propagation on moisture diffusion

$$M_{\Delta\to 1} = M_{\Delta 123\to 1} + M_{\Delta 134\to 1} + M_{\Delta 145\to 1} \tag{9}$$

Besides, the soil on both sides of the crack contacts with the air directly after the cracking and thus exchanges moisture with it. As shown in Fig. 4, the air moisture is assumed to be w_e. Taking Δ123 as an example, the moisture content of the two nodes of the triangular element on the crack boundary is w_1 and w_2. The moisture exchange coefficient between soil and air at the interface is h_c. Then, the moisture exchange between edge 12 of Δ123 and the air in the crack is as follows:

$$\begin{aligned} M_{c12} &= h_c\left(w_e - \frac{w_1 + w_2}{2}\right)L_{12} \\ &= \frac{1}{2}h_c(w_e - w_1)L_{12} + \frac{1}{2}h_c(w_e - w_2)L_{12} \end{aligned} \tag{10}$$

The above moisture mass is allocated to nodes 1 and 2, respectively. The moisture mass allocated to node 1 is given by:

$$M_{c12\to 1} = \frac{1}{2}h_c(w_e - w_1)L_{12} \tag{11}$$

Similarly, the moisture mass into node 1 through edge 15 per unit time is given by

$$M_{c15\to 1} = \frac{1}{2}h_c(w_e - w_1)L_{15} \tag{12}$$

Thus, the total moisture mass into node 1 per unit time is:

$$M_{\text{total}\to 1} = M_{\Delta\to 1} + M_{c12\to 1} + M_{c15\to 1} \tag{13}$$

Substituting Eq. (13) into Eq. (7), the moisture content of node 1 at the next time step can be obtained.

After the crack initiates, the moisture mass of the nodes on both sides of the crack (nodes 1′, 5′, 5, and node 2 in Fig. 4) is calculated in a similar way to that of node 1. For crack tip node 2, it should be noted that the case is slightly special. First, the moisture exchange between five triangular elements directly connected to node 1 is written as:

$$M_{\Delta\to 2} = M_{\Delta 123\to 2} + M_{\Delta 2,12,3\to 2} + M_{\Delta 2,12,11\to 2} + M_{\Delta 2,11,10\to 2} + M_{\Delta 1'28\to 2} \quad (14)$$

As shown in Fig. 5, the moisture mass from air into node 2 includes two parts. The first part is the moisture mass into node 2 from the air through edge 12, referring to Eq. (10), which can be given by:

$$M_{c12\to 2} = \frac{1}{2} h_c (w_e - w_1) L_{12} \quad (15)$$

The second part is the moisture mass into node 2 from the air through edge 1′2, which can be given by

$$M_{c1'2\to 2} = \frac{1}{2} h_c (w_e - w_2) L_{1'2} \quad (16)$$

Thus, the total moisture mass into node 2 per unit time is given by:

$$M_{\text{total}\to 2} = M_{\Delta\to 2} + M_{c1'2\to 2} + M_{c12\to 2} \quad (17)$$

For the nodes not located on cracks, the updating of moisture mass per unit time of these nodes still uses the method in Sect. 3.1. Finally, the moisture content of all the nodes is updated in a similar way as Eq. (7).

3.3 Coupling of moisture diffusion model and mechanical fracture calculation

When moisture starts to decreases, shrinkage and deformation at the surface are greater than that of the soil inside. This inconsistent deformation generates tensile stress in the surface of the soil. Crack is generated when the tensile stress is greater than the tensile strength of the soil, which is known as soil desiccation cracking. In other words, the moisture field affects the stress field. At the same time, crack initiation and propagation affect the moisture migration in the soil. Although cracks prevent the migration of moisture through the crack, moisture can exchange between the soil and the air within the crack.

Thus, the whole coupling of moisture diffusion and mechanical fracture calculation includes the following steps: (1) calculate the moisture distribution of the soil according to the moisture diffusion model; (2) calculate the shrinkage deformation and stress caused by the moisture change and obtain the corresponding equivalent nodal force; (3) the node force caused by shrinkage deformation is added to the total nodal force; (4) the node sharing relationship of adjacent elements on both sides of the crack is updated as the mesh input for the moisture diffusion calculation at the next time step.

According to the above four steps, the problem of soil desiccation cracking can be solved and analyzed. Since steps (1) and (4) have been introduced before, only steps (2) and (3) are introduced next.

With the moisture reduces in the soil, the soil particles gradually get close to each other. At the macro-level, the soil shrinks and generates tensile stress. According to the research results of Hobbs et al. [13], soil particles contact each other and will no longer shrink when the moisture content reaches the shrinkage limit, so the soil volume will not further decrease, as shown in Fig. 6.

Therefore, we suppose that the soil shrinkage deformation is proportional to the change of the moisture content before the moisture content reaches the shrinkage limit

$$\Delta\varepsilon_{ij} = \begin{cases} -\delta_{ij}\alpha(w - w_i), & w \geq w_s \\ -\delta_{ij}\alpha(w_s - w_i), & w < w_s \end{cases} \quad (18)$$

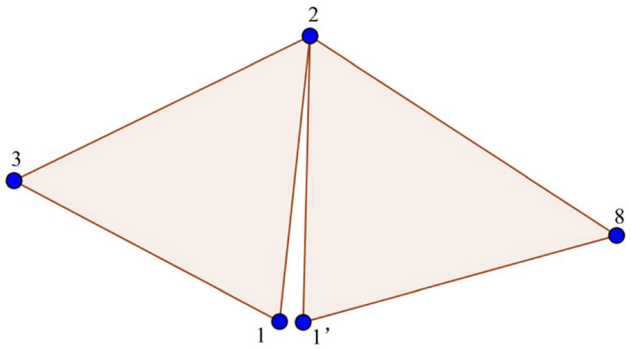

Fig. 5 Calculation diagram of moisture content at crack tip

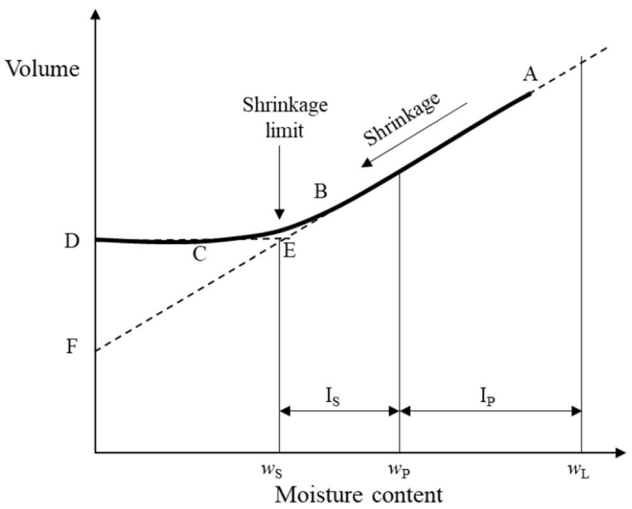

Fig. 6 The relationship between soil volume and moisture content [13] (w_S, shrinkage limit; w_P, plastic limit; w_L, liquid limit; I_S, shrinkage index; I_P, plasticity index)

where α is the shrinkage coefficient, w_i is the initial moisture content (assume $w_i > w_s$), w is the current moisture content, w_s is the shrinkage limit.

It should be noted that the above piece-wisely linear relationship between the soil deformation and moisture content has been supported by experimental tests [13, 52]. If needed, nonlinear relationships, as shown in [50], can be formulated to improve the simulation results.

According to linear elasticity, an equivalent stress increment caused by shrinkage deformation is given by:

$$\Delta\sigma_{ij} = \begin{cases} -\delta_{ij}3K^*\alpha(w - w_i), & w \geq w_s \\ -\delta_{ij}3K^*\alpha(w_s - w_i), & w < w_s \end{cases} \tag{19}$$

where $K^* = 6\mathrm{KG}/(3K + 4G)$ for the plane stress problem and $K^* = K$ for the plane strain problem, K is bulk modulus, and G is the shear modulus. Finally, the equivalent stress increment is applied as nodal forces on the corresponding element.

4 Model validation

4.1 Verification of 1D moisture migration

A rectangular soil strip with a length of 0.1 m and a width of 0.01 m is shown in Fig. 7a and the model is discretized into 80 triangular elements with an element size of 0.005 m as shown in Fig. 7b. The initial moisture content of the model is 0%. To study the soil moisture migration within the soil strip, we apply a flow density of 0.00001 kg/(m^2 s) on the left side of the strip, and the other boundaries are impervious.

The analytical solution of moisture migration in the strip can be written as:

$$w(x,t) = \frac{2q}{k}\left[\left(\frac{\kappa t}{\pi}\right)^{1/2} e^{(-x^2/4\kappa t)} - \frac{x}{2}\mathrm{erfc}\left(\frac{x}{2(\kappa t)^{1/2}}\right)\right] \tag{20}$$

where x is the distance to the left, q is the flow density, t is the time, $\kappa = k/\rho_0$, k is the moisture conductivity tensor, and ρ_0 is the density of soil strip.

Taking $k = 1 \times 10^{-6}$ kg/(m.s), $\rho_0 = 1333$ kg/m^3, the moisture migration in the strip along the x direction at different times is obtained as shown in Fig. 8. It can be seen that the numerical solution is in good agreement with the analytical solution. Figure 9 shows the moisture distribution in the strip at different times. This example verifies the accuracy of the proposed model in dealing with the moisture migration problem.

4.1.1 Effect of element size on moisture migration in the strip

We keep the parameters fixed and study the effect of element size on the moisture migration in the strip. As shown in Fig. 10, three different element sizes are set, which are (a) $L_e = 0.005$ m; (b) $L_e = 0.002$ m; (c) $L_e = 0.001$ m. Figure 11 shows the moisture distribution in the strip with different unit sizes at t = 800,000 s. It can be seen that the element size has little influence on the moisture migration in the strip, which indicates that the proposed model has little dependence on the element size when calculating moisture migration.

4.1.2 Effect of element shape on moisture migration in the strip

Similarly, to study the influence of element shape on the moisture migration in the strip, we set up three different element shapes and keep other parameters unchanged as shown in Fig. 12. Figure 13 shows the moisture distribution in the strip with different element shapes at t = 800,000 s. It can be seen that the element shape also has little influence on the moisture migration in the strip, which indicates that the proposed model has little dependence on the element shape when calculating moisture migration.

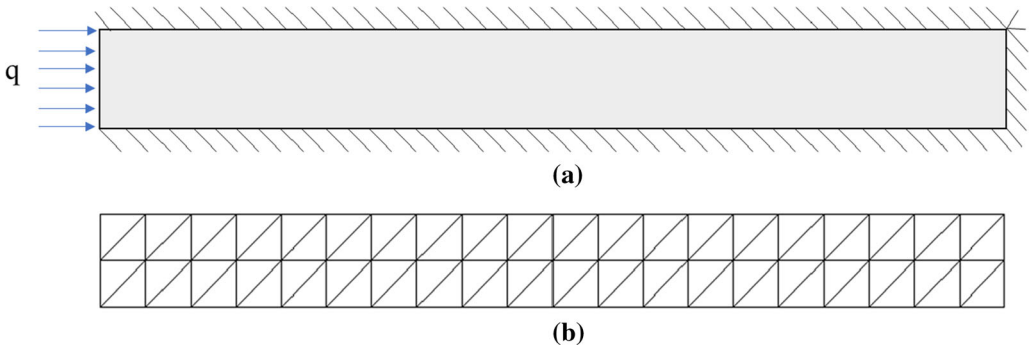

Fig. 7 **a** Calculation model of strip moisture migration; **b** computational mesh, element size $L_e = 0.005$ m

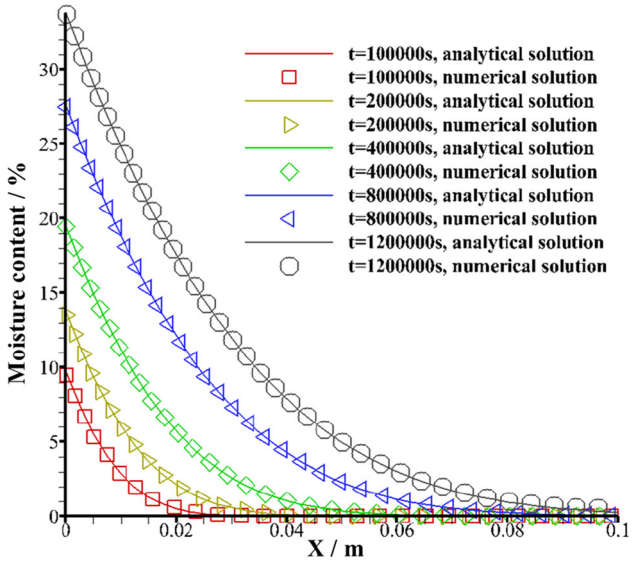

Fig. 8 Comparison of numerical and analytical solutions of moisture migration in the strip

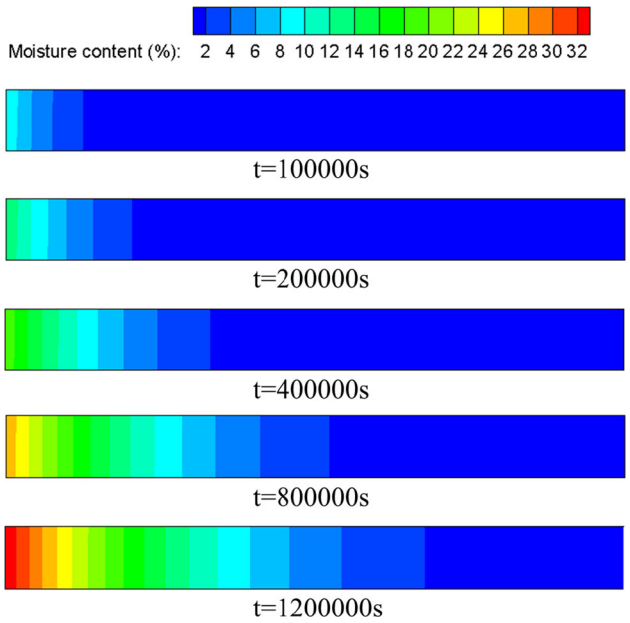

Fig. 9 Moisture distribution in the strip at different times

4.2 Moisture migration of soil with single crack

A rectangular soil with a length of 0.1 m and a width of 0.05 m has a crack through the top, as shown in Fig. 14. The moisture content at the left and the right boundaries is fixed at 100% and 0%, respectively. Since the moisture of the left boundary is higher than that of the right boundary, the moisture in the rectangular soil will migrate from left to right.

The moisture will migrate from left to right uniformly when no crack is encountered as shown in Fig. 14 at t = 100,000 s. However, when the moisture migrates to the crack, it is no longer evenly distributed, as shown in Fig. 14 at t = 200,000 s. As the moisture continues to migrate, the moisture can only be transmitted from the bottom of the crack to the right side of the rectangular soil due to the hindering effect of the crack, so the moisture on the left side of the fracture is always higher than that on the right side as shown in Fig. 14 at t = 500,000 s and t = 1,200,000 s. After the moisture migration is stable, the moisture distribution in rectangular soil is shown as t = 4,000,000 s in Fig. 14.

4.3 Calculation of shrinkage stress and deformation

Take a rectangular soil with $L = 0.1$ m in length and $W = 0.05$ m in width. The top and bottom are fixed in normal direction, but the left and right boundaries are free. The initial moisture content of the rectangular soil is $w_0 = 100\%$. Assuming that the moisture of the rectangular soil reduces to 80% ($\Delta w = 20\%$), the rectangular soil will produce shrinkage deformation. However, because of the constraint of the top and bottom boundaries, the shrinkage deformation along the y direction is constrained and shrinkage stress will produce in soil. The rectangular soil will shrink along the x direction. The analytical solution of this problem is given as follows.

The analytical solution of shrinkage deformation along the x direction is given by:

$$\Delta L_x = L\left(-\frac{v\sigma_y}{E} + \alpha\,\Delta w\right) \tag{21}$$

The shrinkage stress along the y direction is given by:

$$\sigma_y = E\alpha\Delta w \tag{22}$$

The rectangular zone is discretized into 2500 triangular elements with an element size of 0.002 m, as shown in Fig. 15a. The parameters used in the calculation are elastic modulus $E = 1$ MPa, Poisson's ratio $v = 0.2$ and shrinkage coefficient $\alpha = 0.1$. The calculation time step is 20 s.

The displacement vector in the rectangular soil is shown in Fig. 15c. It can be seen that the shrinkage displacement of the rectangular soil only occurs along the x direction, and it gradually decreases from the outside to the inside. The displacement along the y direction is 0. In addition, the displacement distribution of the rectangular soil along the x direction is shown in Fig. 15b, in which the numerical result of the displacement along the x direction is $\Delta L_x = 0.00243102$ m, while the analytical solution obtained according to Eq. (21) is 0.0024 m. The error between the numerical solution and the analytical solution is 1.29%. Figure 15d shows the shrinkage stress of the rectangular soil along the y direction; the numerical result is

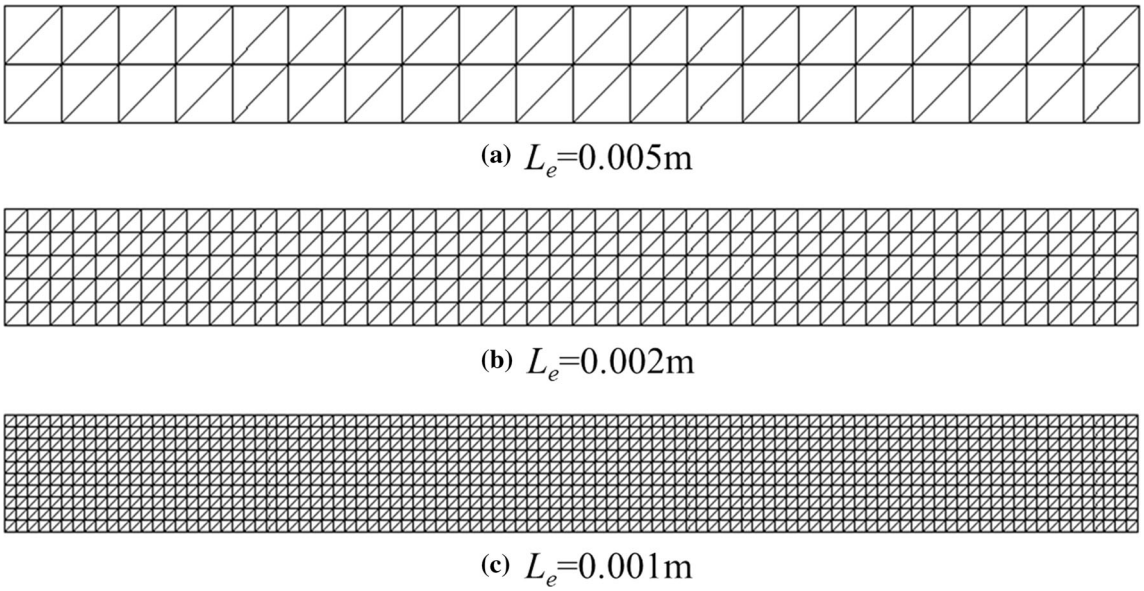

Fig. 10 The rectangular strips are discretized using three different element sizes

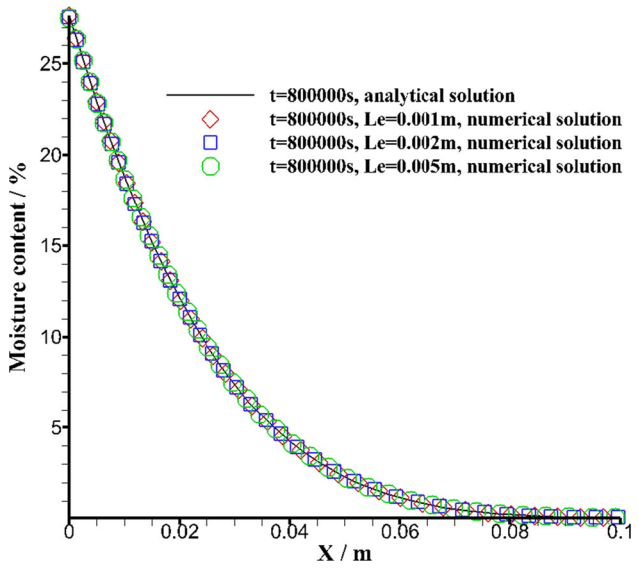

Fig. 11 Effect of different element sizes on moisture migration in the strip

σ_y = 19,630 Pa. The analytical solution obtained according to Eq. (22) is 20000 Pa. The error between the numerical solution and the analytical solution is 1.85%. The numerical results are in good agreement with the analytical solutions, which verifies the accuracy of the proposed model in solving the shrinkage stress and deformation caused by the change of soil moisture.

5 Simulation of soil desiccation cracking

5.1 Simulation results

Peron et al. [35] investigated the desiccation cracking mechanism in a fine-grained soil through experiment. Three types of tests were performed: unconstrained desiccation, linearly constrained desiccation, and crack pattern tests. Three types of materials were used: Bioley silt, Sion silt, and Lafrasse clay. Here, only desiccation tests on Bioley silt under linear constraints are simulated to compare with the experimental results. The Bioley silt properties are: liquid limit w_L = 31.8% and plastic limit w_P = 16.9%, and particles are smaller than 90 μm. The clay minerals in the Bioley silt are illite (10% of the total minerals of mineral species), smectite (10%), and chlorite (5%).

In this experiment, the slurry with an initial moisture content (49.1%) of 1.5 times the liquid limit was poured into an aluminum mold with the size of 295 mm(length) × 49 mm(width) × 12 mm(height), and placed on a base with 2-mm-wide parallel notches, which restrict the horizontal deformation of the soil at the bottom, as shown in Fig. 16a. Under this special constraint condition, only unidirectional cracks are generated in the desiccated soil, as shown in Fig. 16b. The experiment was carried out in a climate chamber with controlled relative humidity and temperature. During the whole test period, the average relative humidity was maintained at 40% with a variation of 4%, and the temperature was fixed at 19 ± 1 °C.

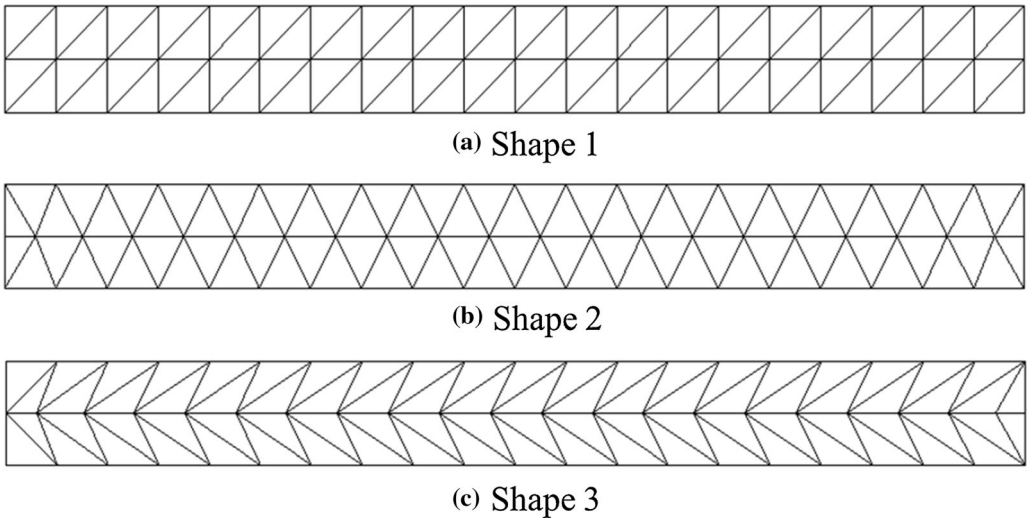

Fig. 12 The rectangular strips are discretized using three different element shapes

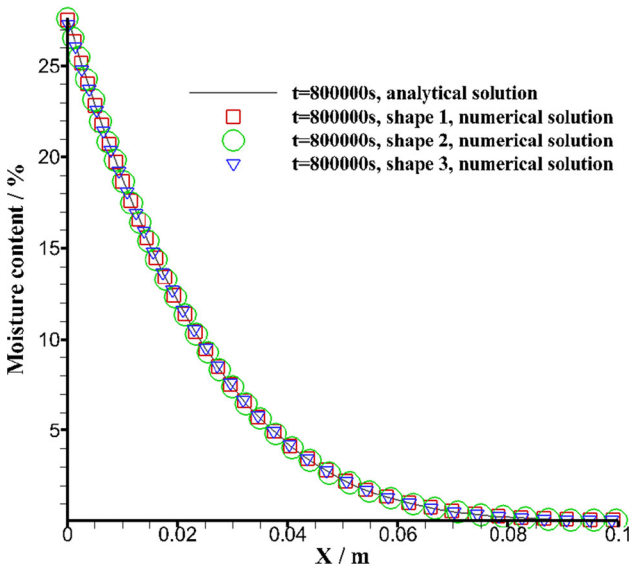

Fig. 13 Effect of different element shapes on moisture migration in the strip

The 2D FDEM-based moisture diffusion–fracture coupling model is used to simulate the experiment of Peron et al. [35] using input parameters listed in Table 1. Throughout the simulation, a flow boundary is prescribed such that the soil loses moisture to its surrounding at a constant flow rate of 6.93×10^{-4} kg/(m^2.min), until the moisture content reaches a residual value of 2.5% in the soil. The dimension of the calculation model is 295 mm (length) × 12 mm (height). Figure 17 is the established model, which is composed of two parts: the soil and the base with notches at the bottom. The width and height of the notches and the spacing between the notches are all 2 mm. Figure 18 shows the soil moisture evolution curves of the experiment and FDEM; it also shows that the moisture content curves of FDEM and experiment are in good agreement. With evaporation of the soil moisture, soil shrinks and induces tensile stress on the surface. When the tensile stress reaches the tensile strength, cracks are formed on the soil surface. With the continuous evaporation of moisture, the cracks propagate along the depth direction gradually and finally reach a stable state. Figure 19a shows the process of crack initiation and propagation in soil desiccation cracking. It can be seen that a total of seven cracks are generated in soil, which is consistent with Peron's experimental results (Fig. 16b). In Fig. 19a, it is also worth noticing that during the desiccation process, moisture distribution is discontinuous across the cracks, showing the influence of crack on moisture migration. It is also interesting to note that, close to crack 1, a small crack initiates from the soil bottom and propagates upward at 2250 min, as shown in Fig. 19a. This phenomenon is also observed in experiment [35] as shown in Fig. 19b and simulation results of similar cases in references [12].

5.2 Soil curling behavior

Drying in the soil can lead to shrinkage, cracking and curling deformation. In this paper, the FDEM-based simulation is used to capture the curling behavior of the soil during desiccation cracking. Figures 20 and 21 illustrate the final vertical and horizontal displacement distribution of the soil. Large horizontal displacement is observed around the crack opening. Due to uneven shrinkage and formation of the crack, the soil also curves upward with a larger vertical displacement around the crack locations, i.e.,

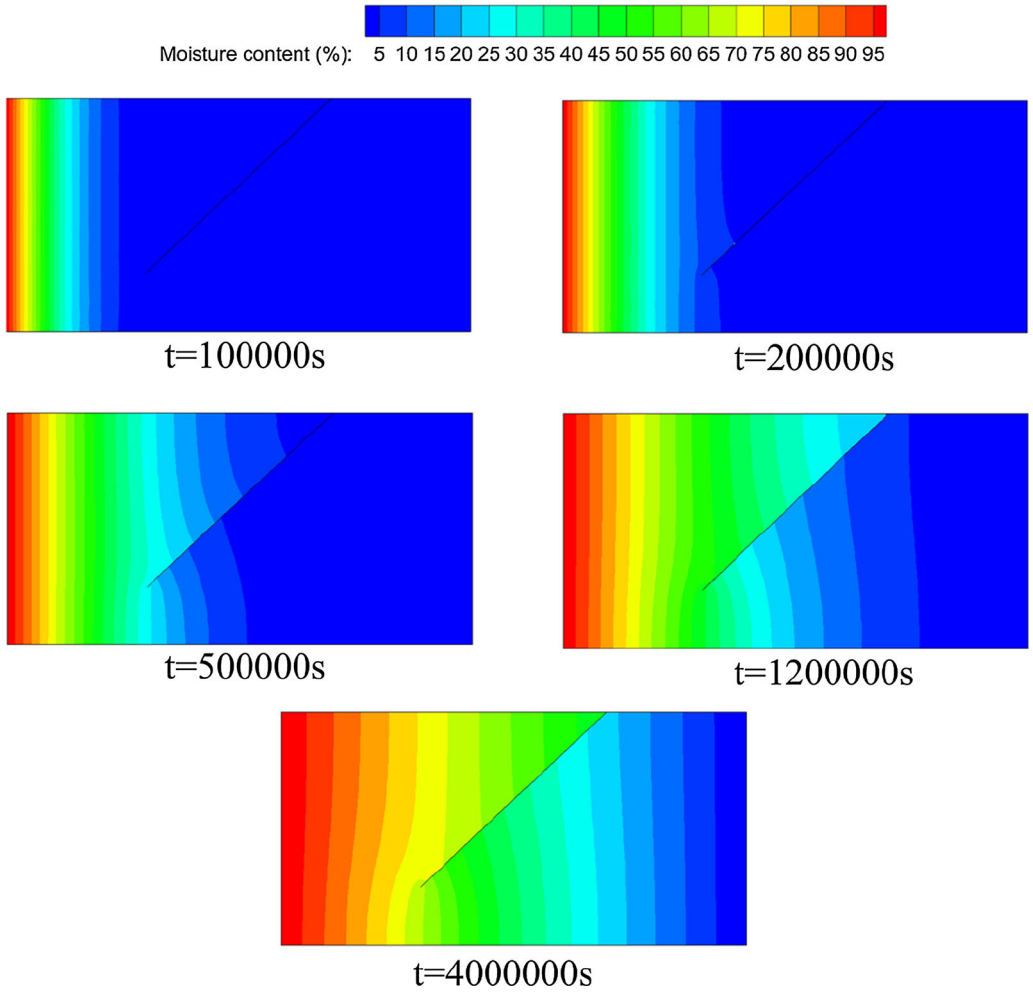

Fig. 14 Moisture distribution in the rectangular soil at different times

soil curling. In addition, the final horizontal displacement at the right end of the soil surface is 6.73×10^{-4} m, which is very close to the numerical simulation of the same experiment (6.64×10^{-4} m) conducted by UDEC [12].

Figure 22 shows the vertical displacements of the soil surface at different times. They indicate that the vertical displacement of the soil surface increases gradually with continuous moisture loss in the soil, and the position of crack initiation is consistent with that of the peak value of the displacement. The large shrinkage in the surface of the soil makes it deform unevenly, resulting in maximum vertical at both ends of the soil sample. When the shrinkage stress is greater than the tensile strength of the soil, cracks begin to occur on the surface of the soil and the soil is cut into many blocks. Due to larger moisture change, shrinkage deformation in the surface is larger than that of the bottom, which makes the soil curls upward between two cracks.

5.3 The evolution pattern of cracks

Cracks initiate after a period of evaporation. We can see from Fig. 19 that the seven cracks (labeled as cracks 1–7) are generated and propagate from surface to the bottom soil gradually with continuous loss of moisture. The original complete soil sample is divided into eight small blocks as shown in Fig. 10 at 2250 min. Figure 23 shows the evolution of the width of seven cracks quantitatively. It can be seen that the initiation time of each crack is quite close but not exactly the same. The crack width increases with the elapse of evaporation time. After 2250 min, the width of all cracks remains stable without further change. It should be noted that the final average width of 7 cracks is 0.841 mm, which is consistent with the experimental results (0.836 mm) [35]. Figure 24 is the evaluation of crack length, which is similar to the numerical result of the literature [56].

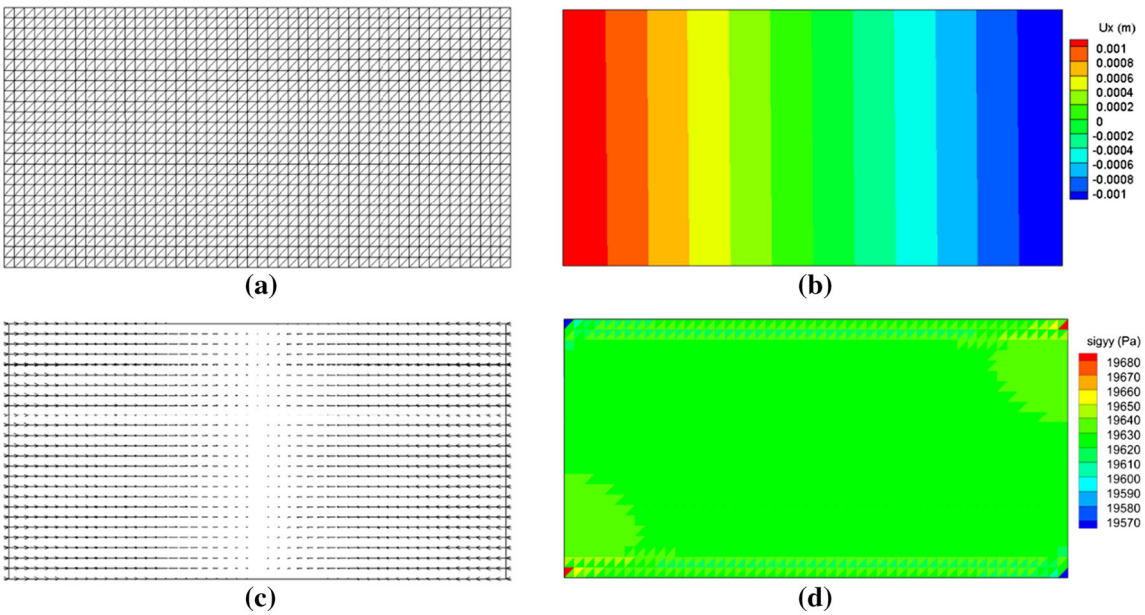

Fig. 15 Calculation of shrinkage stress and deformation of the rectangular soil; **a** the calculation mesh, **b** displacement distribution along the x direction, **c** displacement vector, **d** shrinkage stress distribution

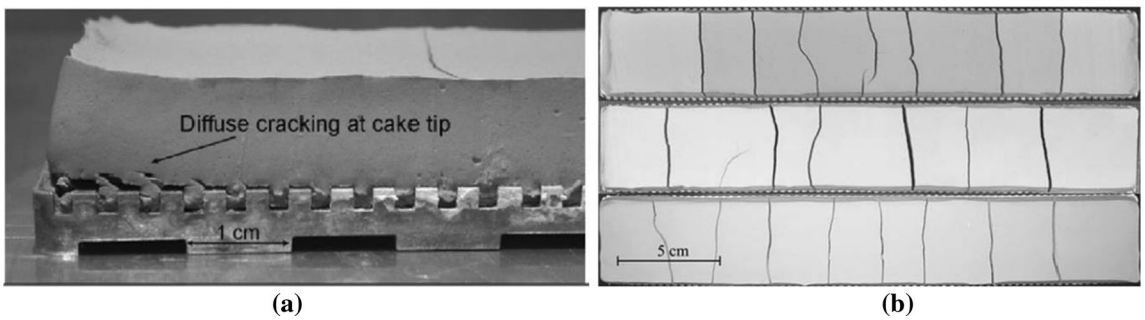

Fig. 16 Drying experiment of saturated clay [35]: **a** View of the aluminum base with notches and (**b**) final crack pattern under the constrained desiccation experiment (viewed from the top)

Table 1 Input parameters in FDEM

Parameters	Soil	Base
Density (kg/m^3)	1.33×10^3	8×10^3
Elastic modulus (MPa)	4.0	2×10^5
Poisson's ratio	0.2	0.2
Tensile strength (kPa)	4.0	10
Friction angle (degree)	20	30
Cohesion (kPa)	10.0	30
Fracture energy release rate, Gf_I (J/m^2)	0.24	–
Fracture energy release rate, Gf_{II} (J/m^2)	10	–
Moisture shrinkage coefficient, α	0.08	–
Moisture conductivity (kg/(m s)), k_m	5×10^{-6}	0

6 Effects of model parameters on soil desiccation cracking

The soil desiccation cracking is affected by many internal and external factors, such as environmental parameters (air temperature, wind speed, and relative humidity) or soil parameters (elastic modulus, moisture shrinkage coefficient, soil thickness). In the following three parts, we investigate the effects of elastic modulus, moisture shrinkage coefficient, and soil thickness on the crack evolution pattern using the 2D moisture diffusion–fracture model.

6.1 Effect of soil elastic modulus

To study the effect of elastic modulus on soil desiccation cracking, we assume the elastic modulus E as 1 MPa,

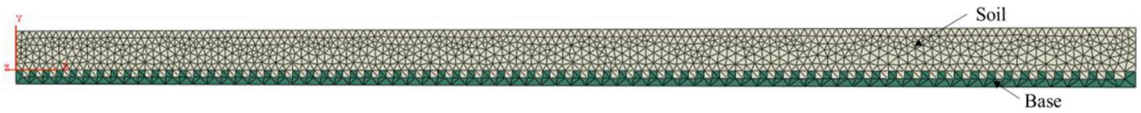

Fig. 17 The calculation mesh for simulating soil desiccation cracking (the upper part is the soil, the lower part is the base with notches)

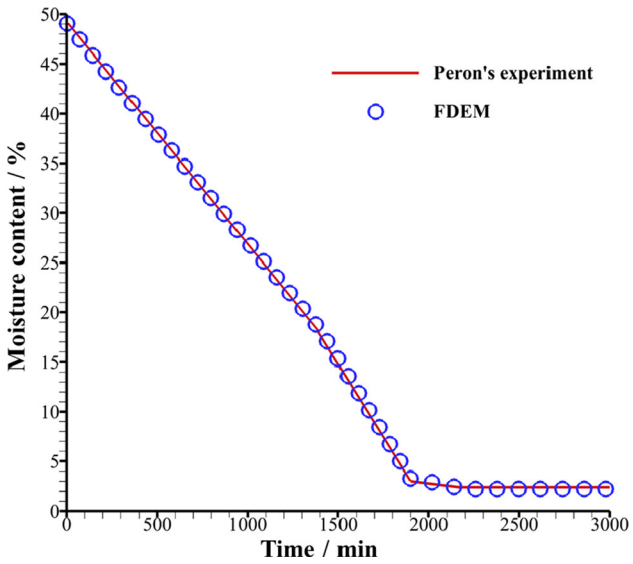

Fig. 18 Evolution of soil moisture content

4 MPa, and 16 MPa, respectively, and keep the other parameters in Table 1 unchanged.

As shown in Fig. 25, the number of cracks increases with the increase in elastic modulus. Figure 26 shows the evolution of the average crack width with time for different E. The larger the elastic modulus is, the earlier the crack initiates. Besides, a larger elastic modulus results in an earlier propagation of the crack to the stable state, with a smaller final averaged crack width. Note that in terms of the total crack width (6.69 mm, 5.89 mm, 4.87 mm for these three cases), when more cracks are generated under a higher E, the soil is less constrained during shrinkage and the accumulated crack width becomes larger.

Figure 27 is the evolution of the averaged crack length for E, which indicates that a larger E leads to an earlier stable state of the averaged crack length. Compared with Fig. 18, the crack reaches a stable state in length before it reaches a stable state in width.

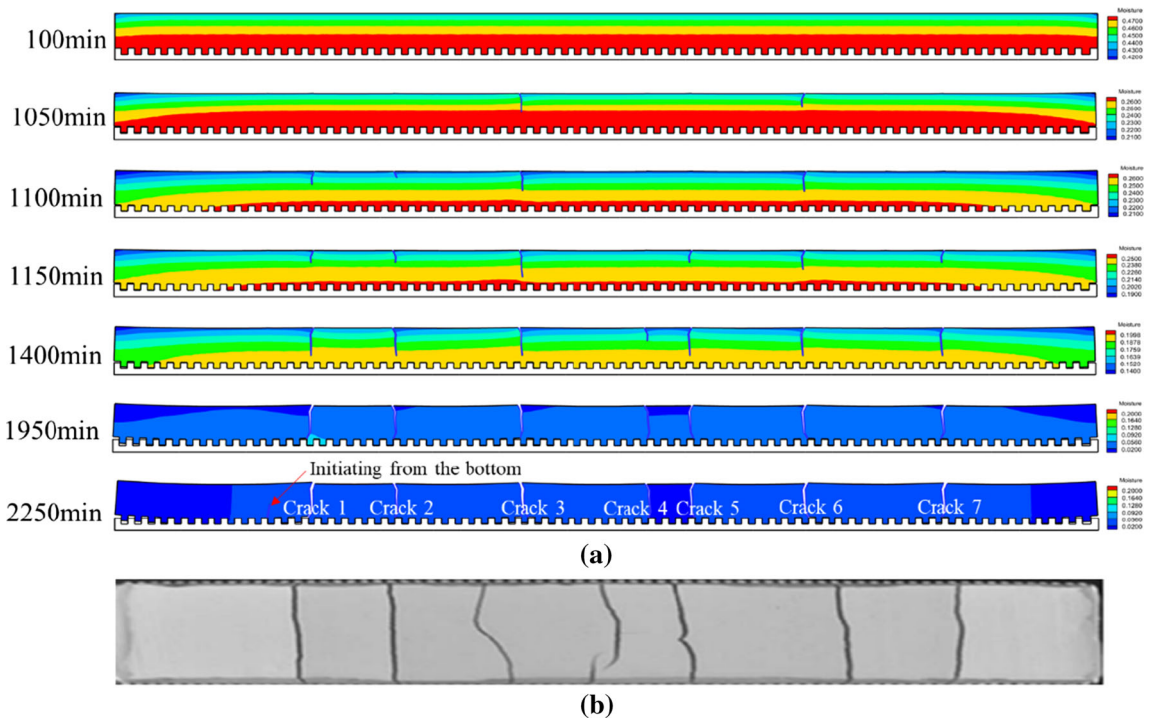

Fig. 19 **a** The process of cracks initiation and propagation in soil desiccation cracking. **b** Desiccation crack from experiment (view on the top)

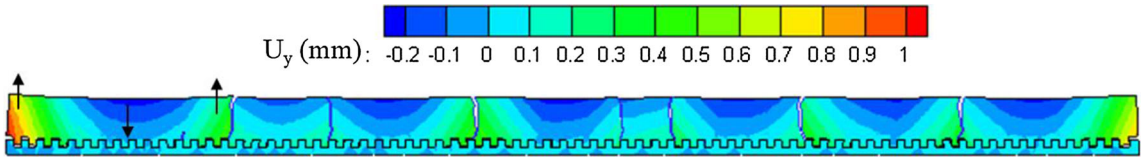

Fig. 20 The final vertical displacement of the soil

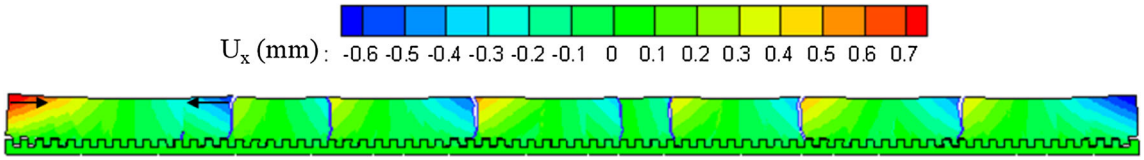

Fig. 21 The final horizontal displacement of the soil

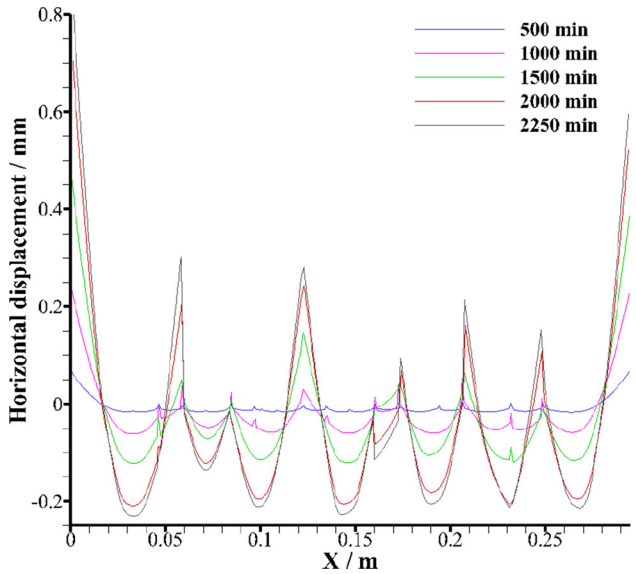

Fig. 22 Vertical displacement of soil surface at different times

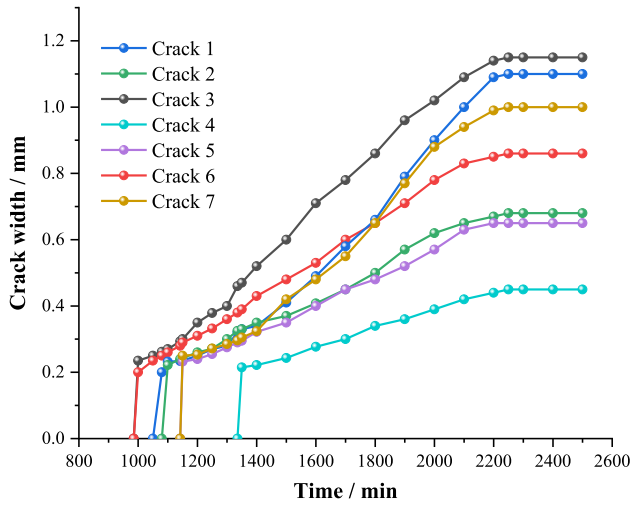

Fig. 23 Evolution curve of crack width

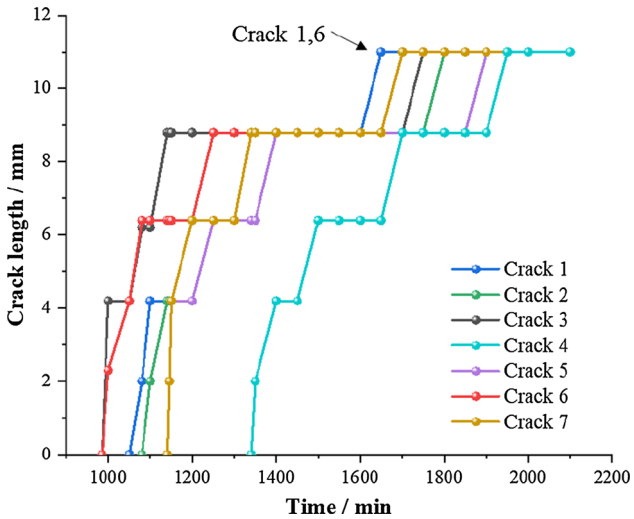

Fig. 24 Evolution curve of crack length

6.2 Effect of moisture shrinkage coefficient

The moisture shrinkage coefficient α of soil is an important factor that affects soil desiccation cracking. Here, we take the moisture shrinkage coefficient as 0.04, 0.08, and 0.12 and keep other parameters unchanged to perform a numerical simulation.

As shown in Fig. 28, the number of cracks increases with an increase in the moisture shrinkage coefficient, which is consistent with the numerical results of the literature [45]. Besides, we can observe that the final averaged crack width is larger for a larger moisture shrinkage coefficient. Evolution analysis of the crack width and length is performed as follows. As shown in Fig. 29, a larger the moisture shrinkage coefficient leads to an earlier crack initiation time. Besides, when the shrinkage coefficient is larger, the crack reaches a stable state earlier with a larger averaged crack width.

According to the experimental results of Tang et al. [48], the surface cracks increase with the clay content of

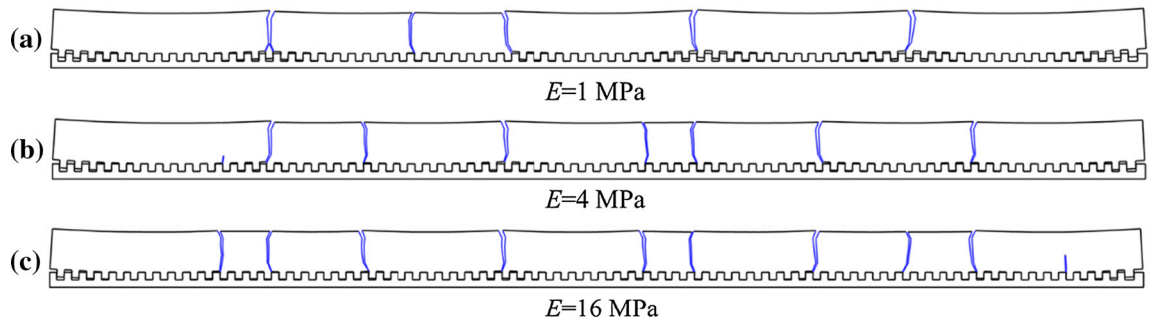

Fig. 25 The final crack patterns for different elastic modulus

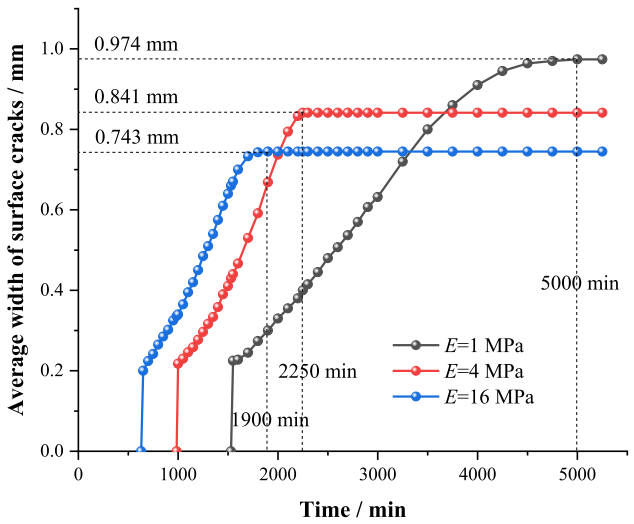

Fig. 26 The evolution of the average crack width for different elastic modulus

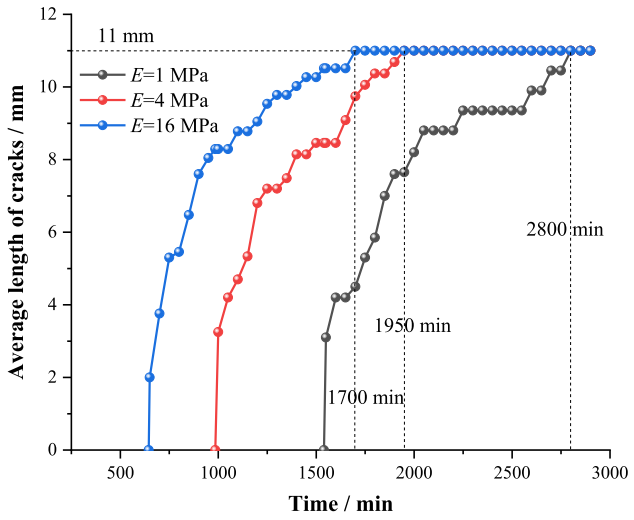

Fig. 27 The evolution of the average crack length for different elastic modulus

the soil. Although the influence of clay content on soil shrinkage cracking is very complex, the high clay content can be expressed by the high value of shrinkage parameter α [45]. The effect of α on soil desiccation cracking in FDEM simulation is consistent with that in experiment.

Figure 30 shows the evolution of the average crack length for different moisture shrinkage coefficients. A larger moisture shrinkage coefficient results in an earlier time for the average crack length to reach the stable state.

6.3 Effect of soil thickness

The soil thickness h is another important factor that affects the final crack pattern of soil desiccation cracking [12, 45, 48]. Here, a series of models are established to study the effect of soil thickness on crack initiation, propagation, and final crack pattern. The model is composed of the soil and the base. The lateral displacement of soil is only constrained by the friction of the soil–base interface (interface friction angle 20°). The length of the soil is 100 mm, while h is taken as 4 mm, 8 mm, and 16 mm, respectively. Moisture exchange only occurs through the top surface of the soil at a constant rate. The parameters are listed in Table 2.

As shown in Fig. 31, the number of cracks decreases with the increase in soil thickness. Besides, we can see that the lateral shrinkage displacements of soil increase with the increase of soil thickness intuitively.

Figure 32 shows the evolution of the average width of these fully penetrating cracks for soil samples with different thicknesses. The average time of crack initiation increases with the increase in sample thickness. The larger the soil thickness, the later the average crack width reaches a stable state. Moreover, the final average crack width increases with the increase in soil thickness. The simulation results are consistent with the numerical results [12, 45] and the experimental results [35, 48].

Figure 33 shows the evolution of the average length of fully penetrating cracks for soil samples with different sample thicknesses. The time for average crack length to

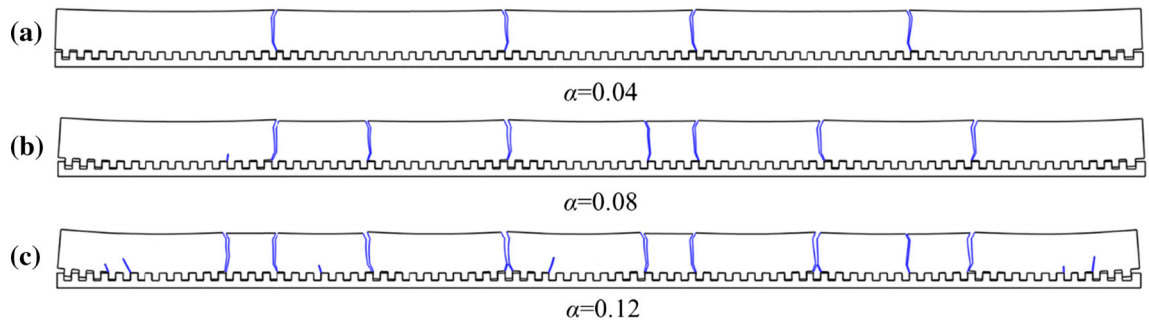

Fig. 28 The final crack pattern for different moisture shrinkage coefficients

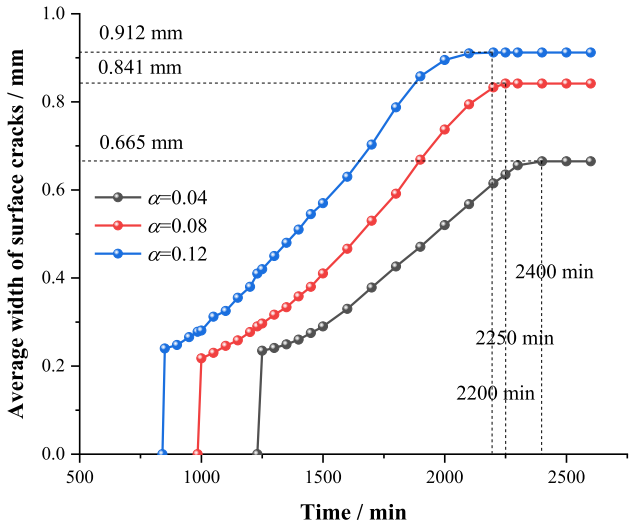

Fig. 29 Evolution of the average crack width for different moisture shrinkage coefficients

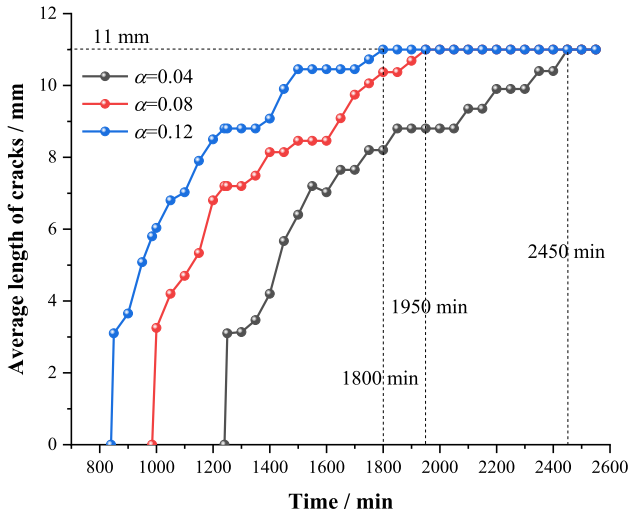

Fig. 30 Evolution of the average crack length for different moisture shrinkage coefficients

Table 2 Input parameters in FDEM for different soil thicknesses

Parameters	Soil	Base
Density (kg/m^3)	1.33 × 10^3	8 × 10^3
Elastic modulus (MPa)	4.0	2 × 10^5
Poisson's ratio	0.2	0.2
Tensile strength (kPa)	4.0	10
Friction angle (degree)	20	30
Cohesion (kPa)	10.0	30
Fracture energy release rate, Gf_I (J/m^2)	0.24	–
Fracture energy release rate, Gf_{II} (J/m^2)	10	–
Moisture shrinkage coefficient, α	0.15	–
Moisture conductivity (kg/(m.s)), k_m	5 × 10^{-6}	0

reach the stability increases with the increase in soil sample thickness.

7 Conclusions

In this paper, a moisture diffusion–fracture coupling model for simulating soil desiccation cracking is established by combining the moisture diffusion model with FDEM mechanical fracture calculation. The coupled model takes into account the evolution of soil moisture content. Meanwhile, the influence of soil cracking on the moisture migration is also considered, that is, the discontinuous distribution of soil moisture content on both sides of the crack is considered in the example of moisture migration of soil with single crack. We use the coupled model to simulate an experiment of soil desiccation cracking. The crack initiation and propagation in soil are well captured in the coupling model. The simulated moisture content evolution, the number of cracks, and the average crack width are all in good agreement with the experimental results, which demonstrates the validity of the moisture diffusion–fracture coupling model. Furthermore, the effects of soil elastic

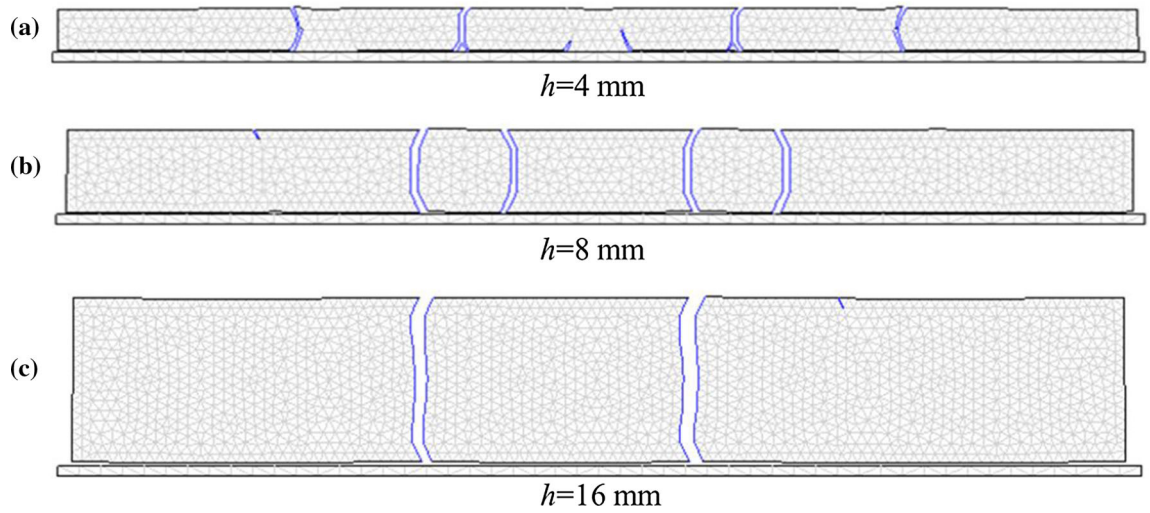

Fig. 31 The final crack pattern for soil samples with different thicknesses

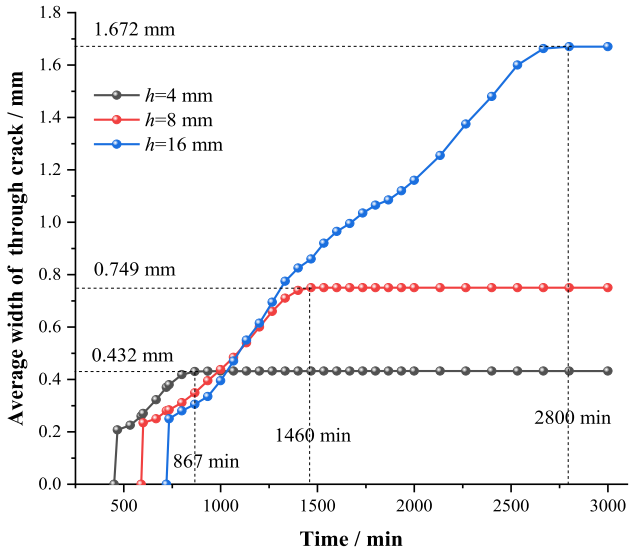

Fig. 32 The evolution of average width of fully penetrating cracks for soil samples with different thicknesses

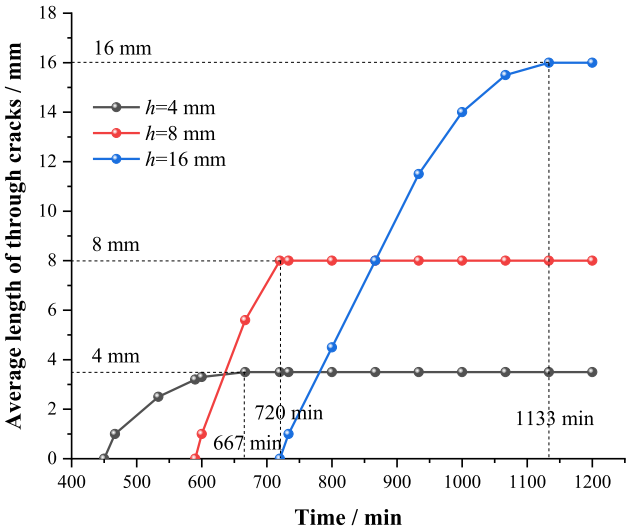

Fig. 33 The evolution of the average length of fully penetrating cracks for soil samples with different thicknesses

modulus, moisture shrinkage coefficient, and soil thickness on the crack evolution pattern are discussed.

The coupled model provides a good quantitative analysis tool for the study of soil desiccation cracking mechanism. Besides, the moisture diffusion model proposed in this paper can also be combined with other common numerical methods such as FEM, DEM, DDA, and NMM to simulate the soil desiccation cracking for a wide range of application.

Acknowledgements This work was supported by the National Natural Science Foundation of China under Grant Nos. 11872340 and 11602006; the Hong Kong Scholars Program (XJ2019040, HKSP19EG04); Hong Kong Research Grants Council grant 16214220; the Fundamental Research Funds for the Central Universities, China University of Geosciences (Wuhan) (CUG170657, CUGGC09).

References

1. Amarasiri AL, Kodikara JK, Costa S (2011) Numerical modelling of desiccation cracking. Int J Numer Anal Meth Geomech 35(1):82–96. https://doi.org/10.1002/nag.894
2. Bagge G (1985) Tension cracks in saturated clay cuttings. In: International conference on soil mechanics and foundation engineering. 11, pp 393–395
3. Bronswijk J, Hamminga W, Oostindie K (1995) Field-scale solute transport in a heavy clay soil. Water Resour Res 31(3):517–526
4. Deng P, Liu Q, Huang X, Liu Q, Ma H, Li W (2021) Acquisition of normal contact stiffness and its influence on rock crack propagation for the combined finite-discrete element method

(FDEM). Eng Fract Mech 242:107459. https://doi.org/10.1016/j.engfracmech.2020.107459
5. Deng G, Shen Z (2006) Numerical simulation of crack formation process in clays during drying and wetting. Geomech Geoeng Int J 1(1):27–41
6. Dyer M, Utili S, Zielinski M (2009) Field study into fine desiccation fissuring at Thorngumbald. Proc ICE Water Manage 162(3):221–232
7. El Mountassir G, Sánchez M, Romero E, Soemitro RAA (2011) Behaviour of compacted silt used to construct flood embankment. Proc Inst Civil Eng Geotech Eng 164(3):195–210. https://doi.org/10.1680/geng.10.00055
8. Farsi A, Xiang J, Latham JP, Carlsson M, Stitt EH, Marigo M (2020) Strength and fragmentation behaviour of complex-shaped catalyst pellets: a numerical and experimental study. Chem Eng Sci 213:115409. https://doi.org/10.1016/j.ces.2019.115409
9. Feng K, Huang D, Wang G (2021) Two-layer material point method for modeling soil–water interaction in unsaturated soils and rainfall-induced slope failure. Acta Geotech. https://doi.org/10.1007/s11440-021-01222-9
10. Fukuda D, Mohammadnejad M, Liu H, Zhang Q, Zhao J, Dehkhoda S, Chan A, Kodama JI, Fujii YJRM, Engineering R (2019) Development of a 3D hybrid finite-discrete element simulator based on GPGPU-parallelized computation for modelling rock fracturing under quasi-static and dynamic loading conditions. Rock Mech Rock End 53:1–34
11. Gui Y, Zhao GF (2015) Modelling of laboratory soil desiccation cracking using DLSM with a two-phase bond model. Comput Geotech 69:578–587. https://doi.org/10.1016/j.compgeo.2015.07.001
12. Gui YL, Zhao ZY, Kodikara J, Bui HH, Yang SQ (2016) Numerical modelling of laboratory soil desiccation cracking using UDEC with a mix-mode cohesive fracture model. Eng Geol 202:14–23. https://doi.org/10.1016/j.enggeo.2015.12.028
13. Hobbs PRN, Jones LD, Kirkham MP, Gunn DA, Entwisle DC (2019) Shrinkage limit test results and interpretation for clay soils. Q J Eng GeolHydrogeol 52(2):220–229. https://doi.org/10.1144/qjegh2018-100
14. Hu LB, Péron H, Hueckel T, Laloui L (2013) Mechanisms and critical properties in drying shrinkage of soils: experimental and numerical parametric studies. Can Geotech J 50(5):536–549. https://doi.org/10.1139/cgj-2012-0065
15. Jones G, Zielinski M, Sentenac P (2012) Mapping desiccation fissures using 3-D electrical resistivity tomography. J Appl Geophys 84:39–51. https://doi.org/10.1016/j.jappgeo.2012.06.002
16. Kodikara J, Barbour SL, Fredlund DG (2000) Desiccation cracking of soil layers. In Proceedings of the first asian conference on unsaturated soils, pp 693–698
17. Kodikara J, Costa S (2013) Desiccation cracking in clayey soils: mechanisms and modelling. In: Multiphysical testing of soils and shales. Springer, pp 21–32
18. Konrad JM, Ayad R (1997) A idealized framework for the analysis of cohesive soils undergoing desiccation. Can Geotech J 34(4):477–488
19. Konrad JM, Ayad R (1997) Desiccation of a sensitive clay: field experimental observations. Can Geotech J 34:929–942
20. Lei Z, Rougier E, Knight EE, Munjiza A, Viswanathan H (2016) A generalized anisotropic deformation formulation for geomaterials. Comput Part Mech 3(2):215–228
21. Li JH, Lu Z, Guo LB, Zhang LM (2017) Experimental study on soil-water characteristic curve for silty clay with desiccation cracks. Eng Geol 218:70–76. https://doi.org/10.1016/j.enggeo.2017.01.004
22. Li JH, Zhang LM (2010) Geometric parameters and REV of a crack network in soil. Comput Geotech 37(4):466–475. https://doi.org/10.1016/j.compgeo.2010.01.006
23. Li JH, Zhang LM (2011) Study of desiccation crack initiation and development at ground surface. Eng Geol 123(4):347–358. https://doi.org/10.1016/j.enggeo.2011.09.015
24. Lisjak A, Liu Q, Zhao Q, Mahabadi OK, Grasselli G (2013) Numerical simulation of acoustic emission in brittle rocks by two-dimensional finite-discrete element analysis. Geophys J Int 195(1):423–443. https://doi.org/10.1093/gji/ggt221
25. Mahabadi O, Kaifosh P, Marschall P, Vietor T (2014) Three-dimensional FDEM numerical simulation of failure processes observed in Opalinus Clay laboratory samples. J Rock Mech Geotech Eng 6(6):591–606. https://doi.org/10.1016/j.jrmge.2014.10.005
26. Mohammadnejad T, Khoei A (2013) Hydro-mechanical modeling of cohesive crack propagation in multiphase porous media using the extended finite element method. Int J Numer Anal Meth Geomech 37(10):1247–1279
27. Munjiza AA (2004) The combined finite-discrete element method. John Wiley & Sons
28. Munjiza A, Andrews K (2000) Penalty function method for combined finite–discrete element systems comprising large number of separate bodies. Int J Numer Meth Eng 49(11):1377–1396
29. Munjiza A, Andrews K, White J (1999) Combined single and smeared crack model in combined finite-discrete element analysis. Int J Numer Meth Eng 44(1):41–57
30. Munjiza AA, Knight EE, Rougier E (2011) Computational mechanics of discontinua. John Wiley & Sons
31. Munjiza A, Knight EE, Rougier E (2015) Large strain finite element method: a practical course. John Wiley & Sons
32. Munjiza A, Owen D, Bicanic N (1995) A combined finite-discrete element method in transient dynamics of fracturing solids. Eng Comput 12(12):145–174
33. Munjiza A, Rougier E, Lei Z, Knight EE (2020) FSIS: a novel fluid–solid interaction solver for fracturing and fragmenting solids. Comput Part Mech 7(5):789–805. https://doi.org/10.1007/s40571-020-00314-9
34. Peron H, Delenne JY, Laloui L, El Youssoufi MS (2009) Discrete element modelling of drying shrinkage and cracking of soils. Comput Geotech 36(1–2):61–69. https://doi.org/10.1016/j.compgeo.2008.04.002
35. Peron H, Hueckel T, Laloui L, Hu LB (2009) Fundamentals of desiccation cracking of fine-grained soils: experimental characterisation and mechanisms identification. Can Geotech J 46(10):1177–1201. https://doi.org/10.1139/t09-054
36. Pouya A (2015) A finite element method for modeling coupled flow and deformation in porous fractured media. Int J Numer Anal Meth Geomech 39(16):1836–1852. https://doi.org/10.1002/nag.2384
37. Pouya A, Vo TD, Hemmati S, Tang AM (2019) Modeling soil desiccation cracking by analytical and numerical approaches. Int J Numer Anal Meth Geomech 43(3):738–763. https://doi.org/10.1002/nag.2887
38. Rodríguez R, Sánchez M, Ledesma A, Lloret A (2007) Experimental and numerical analysis of desiccation of a mining waste desiccation. Can Geotech J 44(6):644–658. https://doi.org/10.1139/t07-016
39. Rougier E, Knight E, Lei Z, Munjiza A (2015) Recent developments in the combined finite-discrete element method. In: 1st Pan-American congress on computational mechanics. p 101
40. Rougier E, Knight EE, Munjiza A (2020) Special issue titled "combined finite discrete element method and virtual experimentation." Comput Part Mech 7(5):763–763. https://doi.org/10.1007/s40571-020-00364-z

41. Sanchez M, Atique A, Kim S, Romero E, Zielinski M (2013) Exploring desiccation cracks in soils using a 2D profile laser device. Acta Geotech 8(6):583–596. https://doi.org/10.1007/s11440-013-0272-1
42. Sánchez M, Manzoli OL, Guimarães LJ (2014) Modeling 3-D desiccation soil crack networks using a mesh fragmentation technique. Comput Geotech 62:27–39
43. Sentenac P, Zielinski M, Baer JU (2009) Clay fine fissuring monitoring using miniature geo-electrical resistivity arrays. Environ Earth Sci 59(1):205–214. https://doi.org/10.1007/s12665-009-0017-5
44. Shan P, Lai X (2019) Mesoscopic structure PFC ~ 2D model of soil rock mixture based on digital image. J Vis Commun Image Represent 58:407–415. https://doi.org/10.1016/j.jvcir.2018.12.015
45. Sima J, Jiang M, Zhou C (2014) Numerical simulation of desiccation cracking in a thin clay layer using 3D discrete element modeling. Comput Geotech 56:168–180. https://doi.org/10.1016/j.compgeo.2013.12.003
46. Sun G, Lin S, Zheng H, Tan Y, Sui T (2020) The virtual element method strength reduction technique for the stability analysis of stony soil slopes. Comput Geotech 119:103349. https://doi.org/10.1016/j.compgeo.2019.103349
47. Tang C-S, Shi B, Liu C, Suo W-B, Gao L (2011) Experimental characterization of shrinkage and desiccation cracking in thin clay layer. Appl Clay Sci 52(1–2):69–77. https://doi.org/10.1016/j.clay.2011.01.032
48. Tang C, Shi B, Liu C, Zhao L, Wang B (2008) Influencing factors of geometrical structure of surface shrinkage cracks in clayey soils. Eng Geol 101(3–4):204–217. https://doi.org/10.1016/j.enggeo.2008.05.005
49. Tatone BS, Grasselli G (2015) A calibration procedure for two-dimensional laboratory-scale hybrid finite–discrete element simulations. Int J Rock Mech Min Sci 75:56–72
50. Trabelsi H, Hadrich B, Guiras H (2018) Evaporation, shrinkage and intrinsic permeability of unsaturated clayey soil: analytical modelling versus experimental data. Arab J Geosci. https://doi.org/10.1007/s12517-018-3507-5
51. Trabelsi H, Jamei M, Zenzri H, Olivella S (2012) Crack patterns in clayey soils: experiments and modeling. Int J Numer Anal Meth Geomech 36(11):1410–1433
52. Trabelsi H, Romero E, Jamei M (2018) Tensile strength during drying of remoulded and compacted clay: the role of fabric and water retention. Appl Clay Sci 162:57–68. https://doi.org/10.1016/j.clay.2018.05.032
53. Tran KM, Bui HH, Sánchez M, Kodikara J (2020) A DEM approach to study desiccation processes in slurry soils. Comput Geotech 120:103448. https://doi.org/10.1016/j.compgeo.2020.103448
54. Tran HT, Wang Y, Nguyen GD, Kodikara J, Sanchez M, Bui HH (2019) Modelling 3D desiccation cracking in clayey soils using a size-dependent SPH computational approach. Comput Geotech 116:103209
55. Vahab M, Khoei A, Khalili N (2019) An X-FEM technique in modeling hydro-fracture interaction with naturally-cemented faults. Eng Fract Mech 212:269–290
56. Vo TD, Pouya A, Hemmati S (2019) Modelling desiccation crack geometry evolution in clayey soils by analytical and numerical approaches. Can Geotech J 56(5):720–729
57. Vo TD, Pouya A, Hemmati S, Tang AM (2017) Numerical modelling of desiccation cracking of clayey soil using a cohesive fracture method. Comput Geotech 85:15–27. https://doi.org/10.1016/j.compgeo.2016.12.010
58. Wang L-L, Tang C-S, Shi B, Cui Y-J, Zhang G-Q, Hilary I (2018) Nucleation and propagation mechanisms of soil desiccation cracks. Eng Geol 238:27–35. https://doi.org/10.1016/j.enggeo.2018.03.004
59. Xu J, Tang X, Wang Z, Feng Y, Bian K (2020) Investigating the softening of weak interlayers during landslides using nanoindentation experiments and simulations. Eng Geol 277:105801. https://doi.org/10.1016/j.enggeo.2020.105801
60. Yan C, Fan H, Huang D, Wang G (2021) A 2D mixed fracture–pore seepage model and hydromechanical coupling for fractured porous media. Acta Geotech. https://doi.org/10.1007/s11440-021-01183-z
61. Yan C, Fan H, Zheng Y, Zhao Y, Ning F (2020) Simulation of the thermal shock of brittle materials using the finite-discrete element method. Eng Anal Boundary Elem 115:142–155. https://doi.org/10.1016/j.enganabound.2020.03.013
62. Yan C, Jiao Y-Y (2018) A 2D fully coupled hydro-mechanical finite-discrete element model with real pore seepage for simulating the deformation and fracture of porous medium driven by fluid. Comput Struct 196:311–326. https://doi.org/10.1016/j.compstruc.2017.10.005
63. Yan C, Jiao YY (2019) A 2D discrete heat transfer model considering the thermal resistance effect of fractures for simulating the thermal cracking of brittle materials. Acta Geotech 15:1–17
64. Yan C, Jiao YY (2019) FDEM-TH3D: a three-dimensional coupled hydrothermal model for fractured rock. Int J Numer Anal Meth Geomech 43(1):415–440
65. Yan C, Jiao Y-Y, Yang S (2019) A 2D coupled hydro-thermal model for the combined finite-discrete element method. Acta Geotech 14(2):403–416. https://doi.org/10.1007/s11440-018-0653-6
66. Yan C, Jiao Y-Y, Zheng H (2018) A fully coupled three-dimensional hydro-mechanical finite discrete element approach with real porous seepage for simulating 3D hydraulic fracturing. Comput Geotech 96:73–89
67. Yan C, Jiao YY, Zheng H (2019) A three-dimensional heat transfer and thermal cracking model considering the effect of cracks on heat transfer. Int J Numer Anal Meth Geomech 43(10):1825–1853. https://doi.org/10.1002/nag.2937
68. Yan C, Ren Y, Yang Y (2020) A 3D thermal cracking model for rockbased on the combined finite–discrete element method. Comput Part Mech 7:881–901. https://doi.org/10.1007/s40571-019-00281-w
69. Yan C, Tong Y (2020) Calibration of microscopic penalty parameters in the combined finite-discrete element method. Int J Geomech 20(7):04020092. https://doi.org/10.1061/(ASCE)GM.1943-5622.0001686
70. Yan C, Wang X, Huang D, Wang G (2021) A new 3D continuous-discontinuous heat conduction model and coupled thermo-mechanical model for simulating the thermal cracking of brittle materials. Int J Solids Struct. https://doi.org/10.1016/j.ijsolstr.2021.111123
71. Yan C, Yang Y, Wang G (2021) A new 2D continuous-discontinuous heat conduction model for modeling heat transfer and thermal cracking in quasi-brittle materials. Comput Geotech. https://doi.org/10.1016/j.compgeo.2021.104231
72. Yan C, Zheng H (2017) A new potential function for the calculation of contact forces in the combined finite-discrete element method. Int J Numer Anal Method Geomech 41(2):265–283. https://doi.org/10.1002/nag.2559
73. Yan C, Zheng H (2016) A two-dimensional coupled hydro-mechanical finite-discrete model considering porous media flow for simulating hydraulic fracturing. Int J Rock Mech Min Sci 88:115–128. https://doi.org/10.1016/j.ijrmms.2016.07.019
74. Yan C, Zheng H (2017) Three-dimensional hydromechanical model of hydraulic fracturing with arbitrarily discrete fracture networks using finite-discrete element method. Int J Geomech 17(6):04016133

75. Yan C, Zheng H (2017) FDEM-flow3D: a 3D hydro-mechanical coupled model considering the pore seepage of rock matrix for simulating three-dimensional hydraulic fracturing. Comput Geotech 81:212–228
76. Yan C, Zheng H (2017) A coupled thermo-mechanical model based on the combined finite-discrete element method for simulating thermal cracking of rock. Int J Rock Mech Min Sci 91:170–178. https://doi.org/10.1016/j.ijrmms.2016.11.023
77. Yan C, Zheng Y, Huang D, Wang G (2021) A coupled contact heat transfer and thermal cracking model for discontinuous and granular media. Comput Methods Appl Mech Eng 375(1):113587. https://doi.org/10.1016/j.cma.2020.113587
78. Yan C, Zheng H, Sun G, Ge X (2016) Combined finite-discrete element method for simulation of hydraulic fracturing. Rock Mech Rock Eng 49(4):1389–1410. https://doi.org/10.1007/s00603-015-0816-9
79. Yao M, Anandarajah A (2003) Three-dimensional discrete element method of analysis of clays. J Eng Mech 129(6):585–596
80. Yu B, El-Zein A (2019) Experimental investigation of the effect of airgaps in preventing desiccation of bentonite in geosynthetic clay liners exposed to high temperatures. Geotext Geomembr 47(2):142–153. https://doi.org/10.1016/j.geotexmem.2018.12.002
81. Zheng Y, Chen C, Liu T, Ren Z (2021) A new method of assessing the stability of anti-dip bedding rock slopes subjected to earthquake. Bull Eng Geol Environ 80(5:):3693–3710. https://doi.org/10.1007/s10064-021-02188-4
82. Zielinski M, Sánchez M, Romero E, Sentenac P (2011) Assessment of water retention behaviour in compacted fills. Proc Inst Civil Eng Geotech Eng 164(2):139–148